ADVANCED ENERGY & SUSTAINABILITY RESEARCH
www.advenergysustres.com

Enhancing Stability of Inverted Perovskite Solar Cells via Buried Interface Modification Using In-Situ Crosslinked Thiol-Ene Polymer

Guorong Zhou, Changzeng Ding, Xin Luo, Lianping Zhang, Zhen Wang, Bo Xu,* and Chang-Qi Ma**

In inverted (p-i-n) perovskite solar cells (PSCs), the buried interface of perovskite has been a thorny issue due to the difficulty of forming a good interfacial contact between hole-transporting layer (HTL) and perovskite. Here, a cross-linkable interfacial layer is induced in p-i-n PSCs to modify the buried interface of perovskite. The cross-linkable layer is copolymerized with pentaerythritol tetrakis(3-mercaptopropionate) (PETMP) and triallyl isocyanato (TAIC) to form cross-linked-PETMP-TAIC. After thermal treatment at 100 °C, the vinyl group in TAIC can react with the thiol group in PETMP to form a cross-linked network. It is found that the cross-linked interfacial layer could not only improve the energy level arrangement between HTL and perovskite, thus promoting the extraction of hole but also significantly enhance the crystalline quality of buried interface of perovskite and inhibit the perovskite phase transition during aging. Devices employing this cross-linkable interfacial layer exhibited a power conversion efficiency of 22.20%, maintaining 86% of its initial efficiency after thermal aging at 85 °C for 500 h.

1. Introduction

ABX_3-type perovskite have numerous excellent optoelectronic properties like tunable optical bandgap, high carrier mobility, and long carrier lifetime.[1–4] In addition, it has a simple preparation process and a wide range of raw material sources. Thus, perovskite solar cells (PSCs) have very promising applications in the fields of large-area photovoltaic power generation, photovoltaic building integration, flexible wearable electronics, and indoor photovoltaics. Currently, the photoelectric conversion efficiency (PCE) of single-junction PSCs has now reached an impressive 27.0%.[5] However, poor stability has always been one of the impediments to the commercialization of PSCs. On the one hand, mixed ionic perovskite is difficult to grow into homogeneous single-crystal films. This is due to the fact that the intermediate phase induces multiple nucleation pathways and therefore generates a large number of grain boundaries, leading to severe non-radiative composite.[6–8] On the other hand, the top and buried interfaces of perovskite polycrystalline films are usually considered to be defect-rich regions, which are the main factors limiting the efficiency and stability improvement of PSCs.[9–11] Currently, most research focuses on the optimization of the surface/interface of perovskite,[12] while a systematic knowledge and in-depth understanding of the buried interface is lacking.

In inverted PSCs, the perovskite buried interface has always been a thorny issue, which is due to the difficulty of forming good interfacial contact between the hole transport layer (HTL) and perovskite layer. Currently, nickel oxide (NiO_X) and self-assembled monolayer (SAM) are often used simultaneously as HTL in inverted PSCs. 2-(3,6-dimethoxy-9 H-carbazol-9-yl) ethyl]phosphonic acid (MeO-2PACz)[13–15] and [2-(9H-carbazol-9-yl)ethyl]phosphonic acid (2PACz)[16,17] are the two most commonly used SAMs. On the one hand, SAM can be densely anchored to NiO_X surface to form a stable interface and passivate defects of NiO_X.[18] On the other hand, the ordered molecules can facilitate hole extraction by generating interfacial dipoles.[19] However, the hydrophobicity of 2PACz leads to poor formation of perovskite film on their surfaces, which can introduce a large number of pinholes and defects. Even though it can be made hydrophilic by methoxyl (-MeO) modification, the substitution

G. Zhou, X. Luo, B. Xu
School of Materials Science and Engineering
Nanjing University of Science and Technology
Nanjing 210094, China
E-mail: boxu@njust.edu.cn

G. Zhou, C. Ding, L. Zhang, Z. Wang, C.-Q. Ma
i-Lab & Printable Electronics Research Center
Suzhou Institute of Nano-Tech and Nano-Bionics
Chinese Academy of Sciences
Suzhou 215123, China
E-mail: czding2017@sinano.ac.cn; cqma2011@sinano.ac.cn

C. Ding
Physics and Center for Functional Materials, Faculty of Science and Technology
Åbo Akademi University
Porthaninkatu 3, 20500 Turku, Finland

The ORCID identification number(s) for the author(s) of this article can be found under https://doi.org/10.1002/aesr.202500027.

DOI: 10.1002/aesr.202500027

of MeO in the carbazole core causes a decrease in the dipole moment, bringing in a large shift between the highest occupied molecular orbital (HOMO) of the SAM and the maximum value of the valence band (VB) of perovskite.[15,16]

Cross-linkable materials (CLMs) have been widely used in traditional engineering plastics and emerging optoelectronic devices, and it can be regarded as the best alternative to organic small molecules or polymers in the pursuit of long-term stability and operational stability of high-performance PSCs.[20,21] To overcome the drawbacks of organic small molecules, cross-linking strategies can fully bind the molecules together through covalent bonds to form a three-dimensional (3D) network, which not only reduces the diffusion coefficient and enhances solvent resistance[22] but also improves the photo/thermal stability and morphology stability. CLMs usually contain highly reactive cross-linkable groups on the molecular skeleton, such as vinyl,[23] acrylate,[24] oxetane,[25] and azide[26] groups. After deposition by solution processing, the cross-linking process can be triggered under certain conditions (heat, light, or initiators) to lock the film morphology and provide a long-term stable environment for PSCs. Li et al[27] inserted a cross-linkable [6,6]-phenyl-C_{61}-butyric acid methyl ester ($PC_{61}BM$) derivative between perovskite/tin oxide (SnO_2). Under UV irradiation, the cross-linked $PC_{61}BM$ not only improved the solvent resistance and UV stability of the device but also optimized the interface between perovskite/electron transport layer (ETL). The cross-linked $PC_{61}BM$-based device showed excellent stability under nitrogen atmosphere and maintains 94% of its initial PCE after aging for 3300 h and negligible loss of device PCE after more than 300 h of UV irradiation. In addition to modifying the interface between perovskite/ETL, the cross-linkable material can also be used to modify the interface between perovskite and hole transport layer. Cross-linkable polyurethanes (CLPU) were recently proposed by Yao[28] et al. as an interfacial layer between perovskite and Spiro-OMeTAD. Considering the multifunctional structure of cross-linked polyurethane, the introduction of this material promoted the secondary crystallization of perovskite grains, which improved the grain size and film quality. In addition, it could inhibit the penetration of external moisture into the perovskite layer. After CLPU modification, the unencapsulated PSCs showed an enhanced stability in $35 \pm 5\%$ RH near 3000 h and in $65 \pm 5\%$ RH over 700 h.

As we mentioned earlier, the perovskite buried interface plays a crucial role in the photovoltaic performance of PSCs. However, the currently known in-situ cross-linking strategies to modify the perovskite buried interface have been utilized in forward devices and have not been used in p-i-n PSCs. Here, we induced a cross-linked interfacial layer in inverted PSCs to modify the buried interface of perovskite. The CL-layer was copolymerized with pentaerythritol tetrakis(3-mercaptopropionate) (PETMP) and triallyl isocyanato (TAIC) to form cross-linked-PETMP-TAIC (CL-PT). After thermal treatment at 100 °C, the vinyl group in TAIC can react with the thiol group in PETMP to form a cross-linked network. It was found that the cross-linked interfacial layer could not only improve the energy level arrangement between SAM and active layer, thus promoting the extraction of hole, but also significantly enhance the crystalline quality of buried interface of perovskite and inhibit the perovskite phase transition during aging. Finally, the modified devices exhibited a highest PCE of 22.20% and improved stability.

2. Result and Discussion

NiO_X + MeO-2PACz has become one of the most used HTL combinations in inverted PSCs. In this work, to further improve the interfacial contact between perovskite and MeO-2PACz and inhibit the phase transition of perovskite, we used an in-situ cross-linking strategy to introduce a cross-linked interfacial layer between perovskite and MeO-2PACz to stabilize the buried interface of perovskite. **Figure 1**a shows the device structure of p-i-n PSCs with CL-PT film deposited on top of the MeO-2PACz. The cross-linking precursor we used, TAIC, contains three vinyl groups, so that the double bonds are easily broken under heating and form a 3D cross-linked network. However, the thermal cross-linking temperatures of most vinyl-based compounds occur above 180 °C,[27,29,30] which would cause severe damage to MeO-2PACz, so finding a low-temperature cross-linking strategy is critical for compatibility between different layers. To lower the cross-linking temperature, a small-molecule PETMP with four thiol groups is selected and mixed with TAIC in a 3:4 molar ratio. In this case, the thiol-ene "click" reaction between the thiol group and the vinyl group occurs under 100 °C heating for 30 min (see Figure 1b for the synthetic routes of CL-PT). To verify the polymerization of CL-PETMP-TAIC on MeO-2PACz surface upon thermal annealing at 100 °C, Fourier transform infrared spectroscopy (FT-IR) was performed on the PETMP, TAIC, and CL-PT films on CaF_2. After cross-linking for 30 min, the peak of -SH stretching vibration at 2570 cm^{-1} had a significant drop, indicating that the thiol group was involved in the cross-linking reaction. The peak of -CH═CH_2 stretching vibration at 3085 cm^{-1}, peaks of -CH and -CH_2 out-of-plane bending vibration at 1689 and 1455 cm^{-1}, separately, disappeared after cross-linking process (Figure 1c). These results indicate that the thiol group undergoes slight reaction under heating conditions, while the vinyl group reacts completely. Figure 1d shows the current density-voltage (J–V) curves of the best triple cations (CsFAMA)-based devices modified with different concentrations of CL-PT, with corresponding photovoltaic parameters—open-circuit voltage (V_{OC}), short-circuit current density (J_{SC}), fill factor (FF), and PCE—summarized in Table S1, Supporting Information. The data indicates that when the concentration of the cross-linking molecule is 1 mg mL^{-1}, the device performance is optimal. As the concentration increases further, both J_{SC} and FF decline sharply, due to an increase in series resistance, which leads to efficiency loss. Compared to the control device, the V_{OC} of the modified device rises from 1.144 to 1.184 V, while the J_{SC} increases from 23.23 to 23.48 mA cm^{-2}, achieving a PCE of 22.20% (compared to 21.50% for the control device). Figure S1, Supporting Information shows the statistical results of device parameters for control and CL-PT modified solar cells.

To gain a deeper understanding of how cross-linked interfacial layer modification influences the morphology and crystallization quality of perovskites, we conducted detailed scanning electron microscopy (SEM) analyses on both the top and buried interfaces of the perovskite films. **Figure 2**a,b present SEM images of the top interface of perovskite films deposited on MeO-2PACz and the cross-linked layer, respectively. Compared with the perovskite grown on MeO-2PACz, which has an average grain size of 0.20 μm, the average grain size of the perovskite grown on CL-PT reaches 0.26 μm, as shown in Figure 2c,d. This indicates

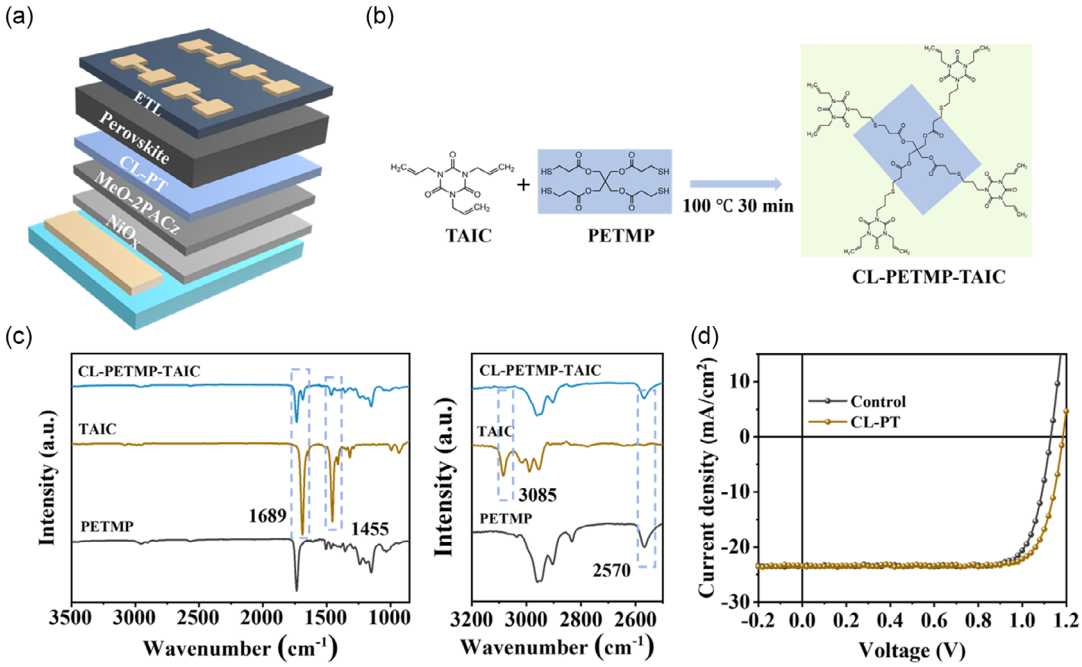

Figure 1. a) Device configuration of CL-PT modified PSC. b) Synthetic routes of CL-PT. c) FT-IR spectra of PETMP, TAIC and CL-PT. d) Illuminated *J–V* characteristics of control device and CL-PT-modified device.

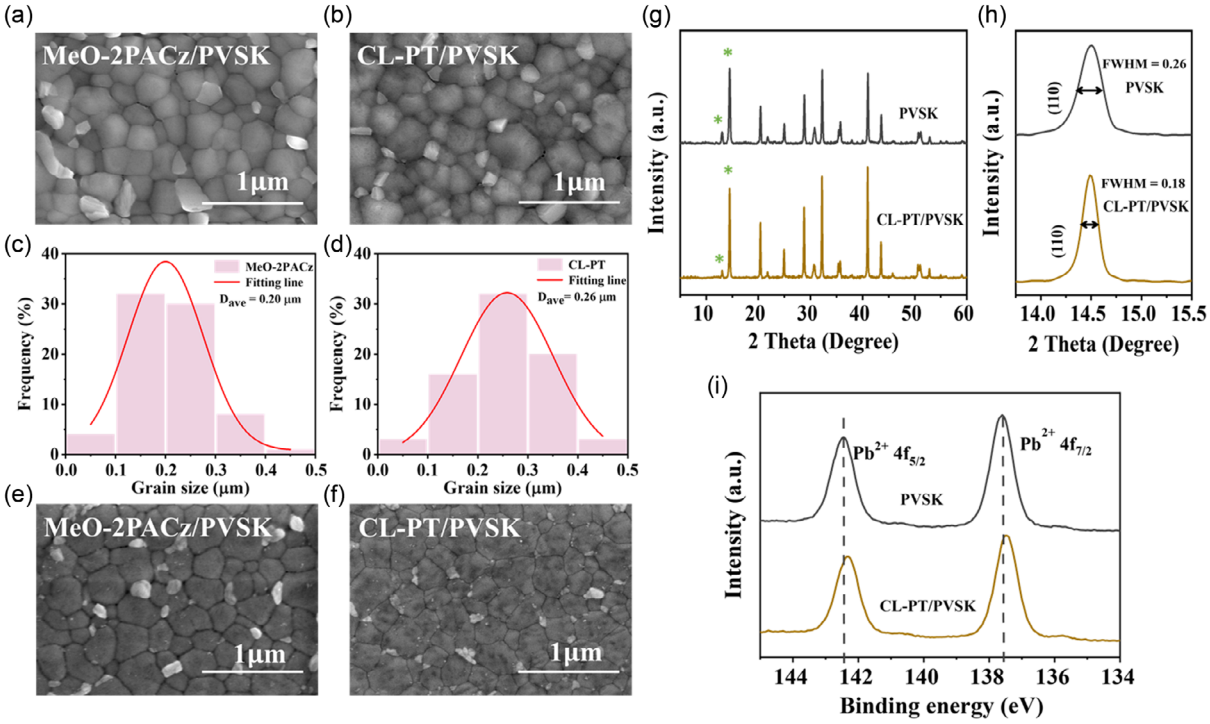

Figure 2. SEM images of a,b) Top interface of perovskite. c,d) The grain size distribution diagram of perovskite. e,f) Buried interface of perovskite. g) XRD spectra of perovskite films deposited on MeO-2PACz and CL-PT. h) Magnified peak of the (110) crystal plane. i) XPS (Pb 4f) spectra of perovskite films deposited on MeO-2PACz and CL-PT.

that the interfacial modification effectively reduces the number of nucleation sites during the nucleation and growth process of the perovskite. It is conducive to the formation of larger perovskite grains and the improvement of film quality. In addition, we used optical UV-curable glue to peel the perovskite films from the MeO-2PACz and CL-PT substrates to characterize the

crystallization of the buried interfaces, as depicted in Figure 2e,f. In perovskites deposited on MeO-2PACz, the grains exhibit larger spacing and a more loosely packed arrangement, leading to a less dense crystal structure. In contrast, perovskite grains grown on the cross-linked interfacial layer show a significantly denser configuration, with grains closely packed together and narrower grain boundaries. This contrast indicates that the cross-linked interfacial layer modification enhances crystallization at the buried interface of perovskite, resulting in a more compact and stable perovskite film. The improved crystallization can reduce interface defects and minimize leakage current, contributing to enhanced optoelectronic performance.

Further structural insights are provided by the X-ray diffraction (XRD) analysis shown in Figure 2g, which compares the crystallization quality of perovskites grown on MeO-2PACz versus those on the cross-linked interfacial layer. The PbI_2 diffraction peak at 13° shows a notable reduction after modification. Simultaneously, the diffraction peak intensity of the (110) crystal plane at 14.5° increases, providing evidence of improved crystallization quality in the modified perovskite structure. Additionally, Gaussian fitting of the (110) crystal plane diffraction peak yields a full width at half maximum (FWHM), which decreases from 0.26 in the unmodified perovskite to 0.18 with the modified layer, as shown in Figure 2h. This reduction in FWHM confirms that the cross-linked interfacial layer has facilitated the growth of perovskite crystals with a more optimal crystallographic orientation, indicating superior crystal quality and potentially higher stability in applications. This set of findings highlights the critical role of cross-linked interfacial layer modification in enhancing the crystallization quality of perovskites. In addition, we performed X-ray photoelectron spectroscopy (XPS) measurements on different perovskite films, as shown in Figure 2i. The Pb 4f XPS spectrum of the control group exhibits two main peaks at 137.6 and 142.45 eV, corresponding to the Pb $4f_{7/2}$ and Pb $4f_{5/2}$ orbitals, respectively. After modification with CL-PT, the Pb 4f peak shifts toward lower binding energy by 0.1 eV, indicating that an interaction occurs between CL-PT and PbI_2. Among them, the thiol groups can form strong coordination with Pb and passivate trap density at the buried interface of the perovskite.[31]

In addition to the effects on perovskite crystallization, the mechanism by which the buried interface enhances charge carrier transport in the device is also a key focus of our research. First, we tested the variation of device's current density with voltage under dark conditions. As shown in **Figure 3**a, after cross-linked layer modification, the device leakage current is significantly reduced, which is attributed to the dense cross-linked film improving the interfacial contact between MeO-2PACz and perovskite and higher crystallization quality of perovskite.[32,33]

Next, we conducted transient photovoltage (TPV) and electrochemical impedance spectroscopy (EIS) tests to analyze the impact of buried interface modification of perovskite on hole extraction and transport in the device. When the laser irradiates the device's surface, photogenerated carriers are produced. Their migration and recombination processes within the device cause a change in surface voltage, allowing us to assess carrier migration and recombination within the device by measuring the voltage difference before and after illumination. Since this study only modified the interface between the hole transport layer and perovskite, we attribute the observed differences solely to hole transport. The fitting results indicate that the TPV decay lifetime of the standard device is 68 µs (Figure 3b), while the decay lifetime of the cross-linked layer-modified device increases to 98 µs,

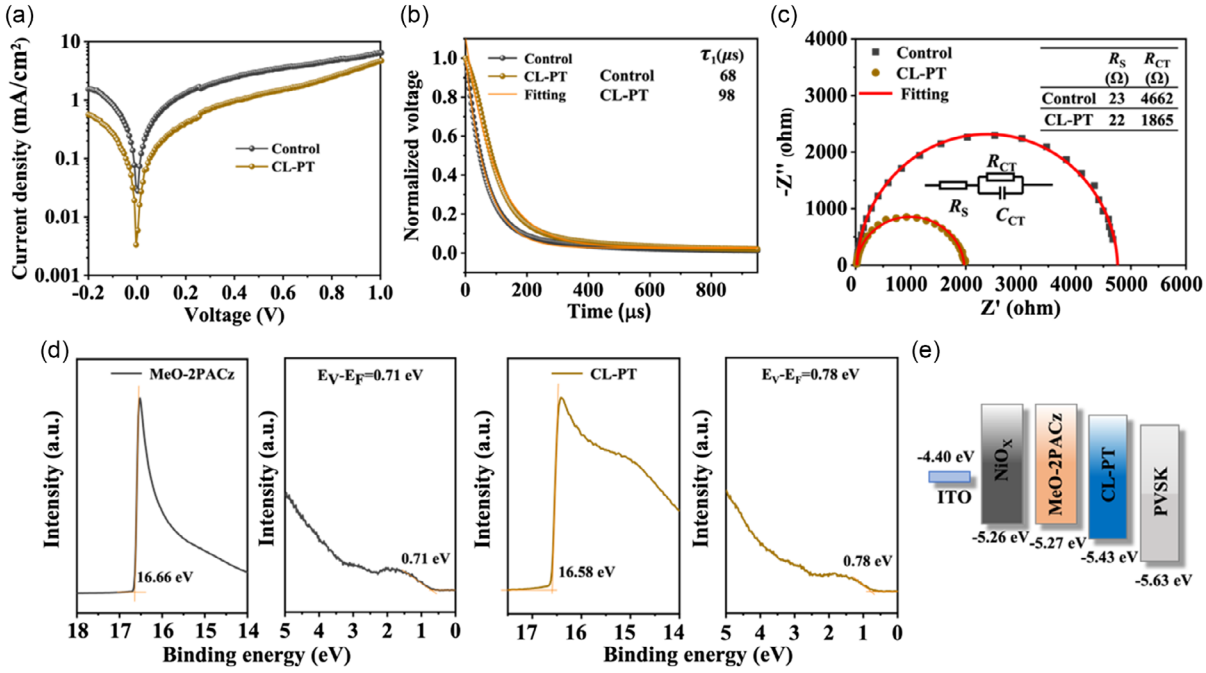

Figure 3. a) Dark-state *J–V* curves of the standard device and the cross-linked layer-modified device. b) TPV decay and fitting curves of the control device and the CL-PT modified device. c) Nyquist plots measured by EIS under dark conditions and the corresponding equivalent circuit model. d) UPS spectra of MeO-2PACz and MeO-2PACz/CL-PT measured under a 10 V bias. e) Energy band diagram of ITO, NiO_X, MeO-2PACz, CL-PT, and the perovskite.

demonstrating that nonradiative recombination during device operation is effectively suppressed, favoring hole extraction. To further explore this phenomenon, we performed EIS tests on the control and cross-linked layer-modified devices under dark conditions. Figure 3c shows the Nyquist plots of both devices, and the corresponding fitted curves were obtained based on an equivalent circuit diagram. In the EIS tests, we mainly focused on the high-frequency component, which indicates the charge transport resistance (R_{CT}).[34] When the R_{CT} of the standard device is 4662 Ω, it decreases to 1865 Ω in the modified device, indicating that the hole transport resistance between perovskite and HTL is reduced after modification, leading to more efficient hole transport and extraction.[35]

Finally, to investigate the effect of the cross-linked layer on device energy level alignment, we performed ultraviolet photoelectron spectroscopy (UPS) tests on NiO_X, MeO-2PACz, and CL-PT (as shown in Figure 3d) and calculated the HOMO levels of them according to formula

$$\mathrm{HOMO} = h\nu - (E_{\mathrm{Cutoff}} - (E_{\mathrm{V}} - E_{\mathrm{F}})) \quad (1)$$

where hν is the UV energy, typically 21.22 eV; E_{Cutoff} is the secondary electron cutoff edge; E_{V} is the valence band maximum; E_{F} is fermi edge. We found the HOMO level of MeO-2PACz to be −5.27 eV and that of CL-PT to be −5.43 eV. It is evident that the introduction of the cross-linked layer could modify the energy

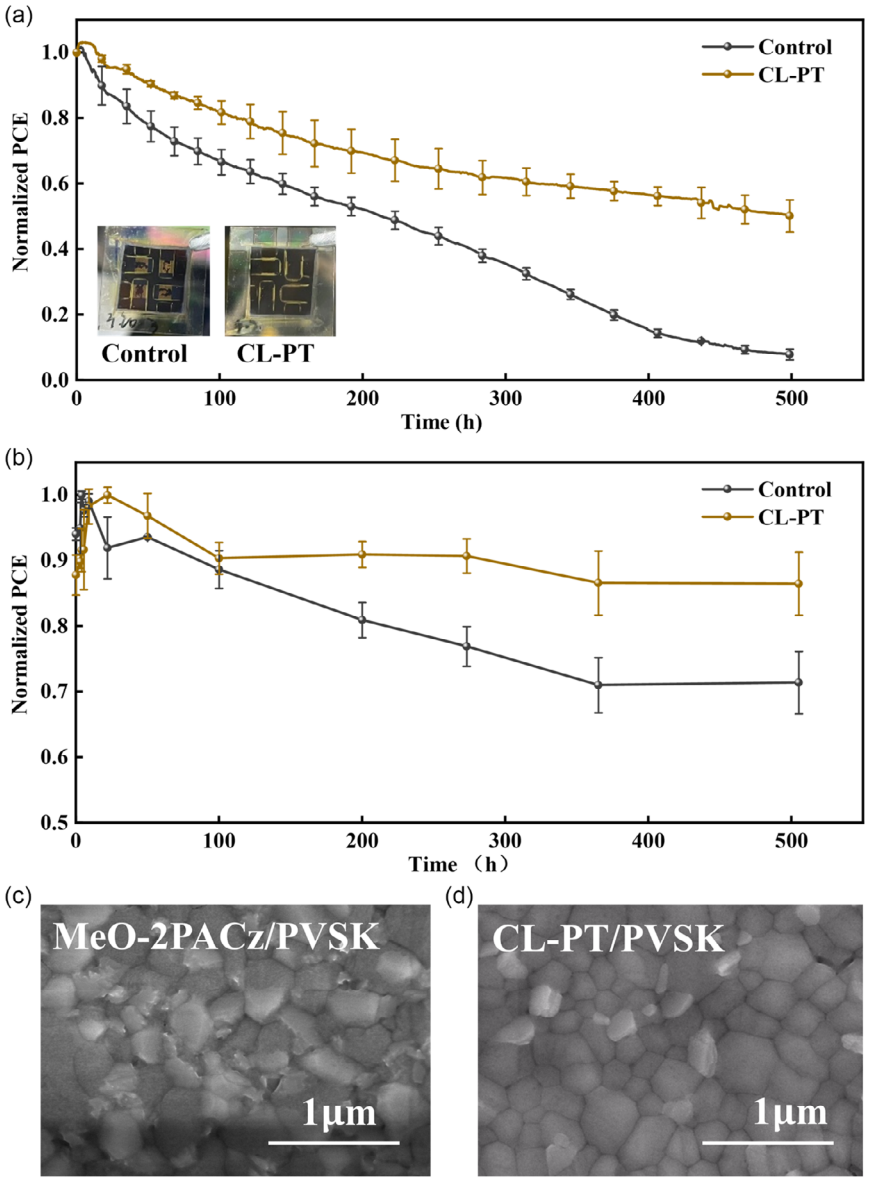

Figure 4. a) MPPT of unencapsulated devices under continuous light illumination at 35 °C in a nitrogen atmosphere. The inset shows photos of control and modified devices after 500 h continuous light illumination. b) Stability test of control and modified devices under 85 °C heating for 500 h in a nitrogen atmosphere. SEM images of aged perovskite (85 °C heating for 500 h) deposited on c) MeO-2PACz and d) CL-PT.

level alignment between MeO-2PACz and the perovskite, reducing the hole injection barrier from the original 0.36 to 0.2 eV. Figure 3e shows the energy level alignment of the device. The reduced hole injection barrier can significantly improve the efficiency of hole transfer from the perovskite to the HTL, making hole extraction smoother. Additionally, the optimized energy level alignment can reduce nonradiative recombination of charges at the interface, thereby minimizing energy loss.[36]

Finally, the operational stability of PSCs was further assessed using maximum power point tracking (MPPT) under continuous LED in a nitrogen environment and without encapsulation. As depicted in **Figure 4**a, after 500 h of continuous illumination, the control device has completely failed, with the PCE approaching zero. In contrast, the device modified with cross-linked layer retained 50% of its initial efficiency, indicating that the cross-linked interfacial layer significantly enhances the operational stability of the device. The *J–V* curves of control and CL-PT-modified devices before and after 500 h of continuous illumination are shown in Figure S2, Supporting Information. A further comparison of the two devices after 500 h of illumination (as shown in the inset of Figure 4a) reveals that the effective area of the control device exhibits severe perovskite phase transition, with substantial lead iodide precipitation. However, in the device modified with the cross-linked layer, lead iodide precipitation occurred only at the electrode edges, with no significant changes in other effective areas. This demonstrates that the cross-linked layer modification could effectively inhibit the perovskite phase transition and significantly improve the device's operational stability.

Besides, we conducted a thermal stability test at 85 °C in a nitrogen atmosphere. In devices with Ag electrodes, due to the reactive nature of Ag, the thermal stability test at 85 °C was limited to 6 h. The changes in various photovoltaic parameters over time during the test are shown in Figure S3, Supporting Information. Compared to unmodified devices, those modified with CL-PT show significantly reduced V_{OC} degradation and a delayed decline in FF. To protect the perovskite from corrosion by the Ag electrode, we further employed a more stable TCO electrode for device aging tests. The changes in V_{OC}, J_{SC}, FF, and PCE over time are shown in Figure S4, Supporting Information. Notably, after cross-linked layer modification, the V_{OC} of the device remained stable even after 500 h of aging, while the V_{OC} of the control device had decayed to 80% of its initial value. This degradation is likely due to the gradual detachment of MeO-2PACz adsorbed on NiO_X during heating, leading to interface failure between MeO-2PACz and the perovskite, which increases non-radiative recombination in the device. In contrast, with the cross-linked layer modification, the buried interface of the perovskite was well protected, suppressing nonradiative recombination at the interface. As shown in the PCE curves in Figure 4b, the control device's PCE declined to below 71% of the initial value after 500 h of aging, whereas the modified device retained 86% of its original efficiency, demonstrating that the cross-linked interfacial layer significantly improves device stability. The *J–V* curves of control and CL-PT-modified devices before and after 500 h of thermal aging are shown in Figure S5, Supporting Information.

To further explore the mechanism by which the cross-linked interfacial layer enhances device stability, we performed SEM analysis on the aged perovskite films, as shown in Figure 4c,d. It is evident that the perovskite film deposited on MeO-2PACz exhibited severe phase transformation after 500 h of aging, with coarse grains and indistinguishable grain boundaries (Figure 4c). In contrast, the perovskite film deposited on the cross-linked layer showed almost no changes after aging (Figure 4d), with a crystalline morphology similar to that before aging. This indicates that the cross-linked interface modification effectively suppresses perovskite phase transformation during thermal aging. Figure S6, Supporting Information shows the XRD pattern of the two perovskite films after 500 h of thermal aging. The diffraction peak intensity at (110) for the perovskite film modified with the cross-linked layer remained higher than that of the control sample, which indicates that after aging, the CL-PT-modified perovskite film retained its initial crystallinity advantage. As discussed previously, the enhanced quality of perovskite film and the passivation effect of CL-PT on the perovskite contribute to outstanding stability of the inverted PSCs.

3. Conclusion

Overall, we selected the vinyl molecule TAIC and the thiol molecule PETMP to undergo in-situ cross-linking under heating conditions, using them as an interfacial modification layer to improve the bottom interface of perovskite in p-i-n perovskite solar cells. The modified devices exhibited a PCE of 22.20% and a V_{OC} of 1.184 V. On one hand, the introduction of the cross-linked interfacial layer improved the crystallization quality of the perovskite buried interface, resulting in a denser perovskite film, which reduced the leakage current of the device. On the other hand, the cross-linked interfacial layer optimized the energy level alignment between MeO-2PACz and the perovskite, lowering the hole transport barrier and thereby suppressing non-radiative recombination in the device, leading to more efficient hole transport. In terms of stability, the modified devices showed significant advantages. After 500 h of thermal aging, they still retained 86% of their initial efficiency. This work marks the first use of an in-situ cross-linking strategy for buried interface modification in p-i-n PSCs, successfully addressing the issue of interface instability between MeO-2PACz and perovskite, providing a new direction for achieving efficient and stable solar cells.

4. Experimental Section

Materials: Lead (II) iodide (PbI_2) and lead (II) bromide ($PbBr_2$), cesium Iodide (CsI), formamidinium iodide (FAI), methylammonium bromide (MABr), phenethylammonium iodide (PEAI), and bathocuproine (BCP) were purchased from Xi'an Polymer Light Technology in China. NiO_X nanoparticle powder and $PC_{61}BM$ were purchased from Advanced Election Technology Company in China. MeO-2PACz was purchased from TCI AMERICA in China. TAIC was purchased from Energy Chemical. PETMP was purchased from Bidepharm. Dimethylformamide (DMF, purity >99%), dimethyl sulfoxide (DMSO, purity >99%), ethanol, isopropyl alcohol (IPA, purity >99%), and chlorobenzene (CB, purity >99%) were purchased from J&K scientific. All materials were used directly.

Instruments and Characterization: The *J–V* characters of solar cells were measured with a Keithley 2400 source meter in an N_2 glove box under a simulated sun AM 1.5 G (Newport VeraSol- 2 LED Class AAA Solar Simulator). SEM images were gained by a field-emission scanning electron microscope (S-4800) under an accelerating voltage of 5 kV. Fourier transform infrared spectroscopy (FT-IR) was characterized using a Fourier

transform infrared spectrometer (ThermoFisher NICOLET IS10). In this test, different samples were deposited on CaF_2 glass and then tested. Ultraviolet photoelectron spectroscopy (UPS) and X-ray photoelectron spectroscopy (XPS) were tested using a PHI 5000 VersaProbe X-ray photoelectron spectrometer. The X-ray diffraction pattern (XRD) was characterized using a Bruker D8 Advance X-ray diffractometer. Electrical impedance spectroscopy (EIS) was conducted on the electrochemical workstation (PGSTA302N). The EIS measure conditions were under dark and applied bias at open voltage, the frequency range is 0.1–10 MHz. Transient photovoltage (TPV) was carried out on the Comprehensive Test Instrument from National Instruments.

Preparation of Device: ITO glass substrate was cleaned by sequentially washing with detergent, deionized water (twice), and ethanol (twice). Before use, the ITO was treated by ultraviolet ozone for 30 min. Then, a thin layer of NiO_X nanoparticle film (20 mg mL^{-1} NiO_X water solution) was deposited on ITO substrate by spin coating at 4000 rpm for 30 s, and annealed in ambient air at 150 °C for 20 min. 0.5 mg mL^{-1} MeO-2PACz was deposited on the NiO_X at 4000 rpm for 30 s, and annealed at 100 °C for 10 min. 1 mg mL^{-1} CL-PT (0.673 mg of TAIC and 1 mg of PETMP were dissolved in 1673 µL of CB) was coated on MeO-2PACz surface at 4000 rpm for 30 s, and annealed at 100 °C for 30 min. For $Cs_{0.05}(FA_{0.85}MA_{0.15})_{0.95}Pb(I_{0.85}Br_{0.15})_3$ perovskite films, 1.2 M perovskite precursor solution was prepared through dissolving 190.12 mg FAI, 548.6 mg PbI_2, 77.07 mg $PbBr_2$, 21.84 mg MABr, and 17.68 mg CsI in mixed solvents of DMF and DMSO (v/v: 4:1). The perovskite precursor solution was spin-coated on substrate at 5000 rpm for 30 s, 230 µL EA was dropped into the perovskite film at 10 s before ending the program, then the perovskite films were annealed at 120 °C for 30 min. After that, 1 mg mL^{-1} PEAI (dissolved in IPA) was coated on the perovskite surface at 5000 rpm for 20 s and annealed at 100 °C for 10 min, then 20 mg ml^{-1} of $PC_{61}BM$ (dissolved in CB) was spin-coated at 3000 rpm 30 s. Afterward, the BCP solution in IPA (0.5 mg mL^{-1}) was spin-coated on $PC_{61}BM$ film at 5000 rpm for 30 s. Finally, 100 nm Ag electrode was thermally evaporated on the BCP film under vacuum of 5×10^{-4} Pa.

Preparation of SEM Samples: For SEM measurement on buried interface of perovskite, the perovskite film was deposited on different substrates, and UV-curable adhesive was applied to the surface of perovskite. Subsequently, the adhesive was cured for 10 min through a UV curing process, and then the perovskite film was peeled off to expose the buried interface.

Operational Stability Test: Operational stability of the cells were performed on a multi-channel solar cell performance decay testing system (PVLT-G8001M, Suzhou D&R Instruments Co. Ltd.) inside a N_2-filled glove box (H_2O <10 ppm, O_2 <10 ppm), and the cells were illuminated with a white LED light (D&R Light, L-W5300KA-150, Suzhou D&R Instruments Co. Ltd.) at a simulated one sun intensity (the initial short current equals to the J_{SC} measured under standard condition). The cell's performance was measured by *I–V* sweeping from 1.2 to −0.2 V, with a step of 0.01 V. The temperature was set at 25 °C. *J–V* characteristics of the cells were measured periodically, and the maximum power output point (mpp) was calculated automatically. An external resistor that matches the mpp point ($R = I_{max}/V_{max}$) was then attached to the cells in between *J–V* sweepings according to the *J–V* sweeping results so that the recorded PCE decay curves directly reflect the performance decay of the cells under the simulated operational situation.

Supporting Information

Supporting Information is available from the Wiley Online Library or from the author.

Acknowledgements

The authors would like to acknowledge the financial support from National Natural Science Foundation of China (grant no. 22409208), Jiangsu Science and Technology Program (grant no. BE2022021), China Postdoctoral Science Foundation (grant nos. 2023T160469 and 2023M732554), the Ministry of Science and Technology (grant no. 2023YFB4204504), Natural Science Foundation of Jiangsu Province (grant no. BK20240083), National Natural Science Foundation of China (grant nos. W2412114, 22279059). The authors are grateful for the technical support from the Suzhou Institute of Nano-Tech and Nano-Bionics for the XPS/UPS testing in Nano-X.

Conflict of Interest

The authors declare no conflict of interest.

Author Contributions

Guorong Zhou: data curation (lead); investigation (lead); writing—original draft (lead). **Changzeng Ding**: formal analysis (equal); funding acquisition (lead); writing—original draft (equal); writing—review and editing (lead). **Xin Luo**: data curation (equal); formal analysis (equal). **Lianping Zhang**: data curation (equal); writing—original draft (equal). **Zhen Wang**: formal analysis (equal); writing—original draft (equal). **Bo Xu**: funding acquisition (lead); project administration (equal); supervision (equal); writing—review and editing (lead). **Chang-Qi Ma**: conceptualization (lead); funding acquisition (lead); project administration (lead); supervision (lead); writing—review and editing (lead).

Data Availability Statement

The data that support the findings of this study are available from the corresponding author upon reasonable request.

Keywords

buried interface, cross-linkable molecules, perovskite solar cells, power conversion efficiency, thermal stability

Received: February 14, 2025
Revised: March 15, 2025
Published online: April 4, 2025

[1] J. H. Noh, S. H. Im, J. H. Heo, T. N. Mandal, S. I. Seok, *Nano Lett.* **2013**, *13*, 1764.
[2] A. Kojima, K. Teshima, Y. Shirai, T. Miyasaka, *J. Am. Chem. Soc.* **2009**, *131*, 6050.
[3] C. C. Stoumpos, C. D. Malliakas, M. G. Kanatzidis, *Inorg. Chem.* **2013**, *52*, 9019.
[4] G. Xing, N. Mathews, S. Sun, S. S. Lim, Y. M. Lam, M. Grätzel, S. Mhaisalkar, T. C. Sum, *Science* **2013**, *342*, 344.
[5] J. Zhou, L. Tan, Y. Liu, H. Li, X. Liu, M. Li, S. Wang, Y. Zhang, C. Jiang, R. Hua, *Joule* **2024**, *8*, 1691.
[6] M. Abbas, X. Xu, M. Rauf, A. K. K. Kyaw, *Photonics* **2024**, *11*, 87.
[7] J. W. Lee, S. H. Bae, N. De Marco, Y. T. Hsieh, Z. Dai, Y. Yang, *Mater. Today Energy* **2018**, *7*, 149.
[8] F. Wang, S. Bai, W. Tress, A. Hagfeldt, F. Gao, *npj Flexible Electron.* **2018**, *2*, 22.
[9] Z. Zhang, W. Kim, M. J. Ko, Y. Li, *Nano Converg.* **2023**, *10*, 23.
[10] B. Xiao, X. Li, Y. Qian, Z. Yi, A. Y. Haruna, Q. Jiang, Y. Luo, J. Yang, *Appl. Surf. Sci.* **2022**, *604*, 154431.
[11] J. Cheng, H. Cao, S. Zhang, F. Yue, Z. Zhou, *Mater. Chem. Front.* **2024**, *8*, 956.
[12] W. Yang, B. Ding, Z. Lin, J. Sun, Y. Meng, Y. Ding, J. Sheng, Z. Yang, J. Ye, P. J. Dyson, M. K. Nazeeruddin, *Adv. Mater.* **2023**, *35*, e2302071.

[13] A. R. Alghamdi, M. Yanagida, Y. Shirai, G. G. Andersson, K. Miyano, *ACS Omega* **2022**, *7*, 12147.
[14] J. Sun, C. Shou, J. Sun, X. Wang, Z. Yang, Y. Chen, J. Wu, W. Yang, H. Long, Z. Ying, *Solar RRL* **2021**, *5*, 2100663.
[15] A. Al Ashouri, A. Magomedov, M. Roß, M. Jošt, M. Talaikis, G. Chistiakova, T. Bertram, J. A. Márquez, E. Köhnen, E. Kasparavičius, S. Levcenco, L. Gil-Escrig, C. J. Hages, R. Schlatmann, B. Rech, T. Malinauskas, T. Unold, C. A. Kaufmann, L. Korte, G. Niaura, V. Getautis, S. Albrecht, *Energy Environ. Sci.* **2019**, *12*, 3356.
[16] L. Li, Y. Wang, X. Wang, R. Lin, X. Luo, Z. Liu, K. Zhou, S. Xiong, Q. Bao, G. Chen, Y. Tian, Y. Deng, K. Xiao, J. Wu, M. I. Saidaminov, H. Lin, C. Q. Ma, Z. Zhao, Y. Wu, L. Zhang, H. Tan, *Nat. Energy* **2022**, *7*, 708.
[17] J. Lin, Y. Wang, A. Khaleed, A. A. Syed, Y. He, C. C. S. Chan, Y. Li, K. Liu, G. Li, K. S. Wong, J. Popovic, J. Fan, A. M. C. Ng, A. B. Djurisic, *ACS Appl. Mater. Interfaces* **2023**, *15*, 24437.
[18] D. S. Mann, P. Patil, S. N. Kwon, S. I. Na, *Appl. Surf. Sci.* **2021**, *560*, 149973.
[19] H. Zhang, N. G. Park, *DeCarbon* **2024**, *3*, 100025.
[20] C. Gao, D. Shi, C. Li, X. Yu, X. Zhang, Z. Liu, G. Zhang, D. Zhang, *Adv. Sci.* **2022**, *9*, e2106087.
[21] Z. Ma, B. Zhao, H. Gao, Y. Gong, R. Yu, Z. A. Tan, *J. Mater. Chem. A* **2022**, *10*, 18542.
[22] Y. Bai, Q. Dong, Y. Shao, Y. Deng, Q. Wang, L. Shen, D. Wang, W. Wei, J. Huang, *Nat. Commun.* **2016**, *7*, 12806.
[23] S. Daskeviciute-Geguziene, M. A. Truong, K. Rakstys, M. Daskeviciene, R. Hashimoto, R. Murdey, T. Yamada, Y. Kanemitsu, V. Jankauskas, A. Wakamiya, V. Getautis, *ACS Appl. Mater. Interfaces* **2024**, *16*, 1206.
[24] Z. Zhu, D. Zhao, C. C. Chueh, X. Shi, Z. Li, A. K. Y. Jen, *Joule* **2018**, *2*, 168.
[25] Y. Wu, G. Xu, J. Xi, Y. Shen, X. Wu, X. Tang, J. Ding, H. Yang, Q. Cheng, Z. Chen, Y. Li, Y. Li, *Joule* **2023**, *7*, 398.
[26] W. Qiu, J. P. Bastos, S. Dasgupta, T. Merckx, I. Cardinaletti, M. V. C. Jenart, C. B. Nielsen, R. Gehlhaar, J. Poortmans, P. Heremans, I. McCulloch, D. Cheyns, *J. Mater. Chem. A* **2017**, *5*, 2466.
[27] Z. Li, N. Liu, Z. Liu, X. Wang, Y. Hu, Q. Xu, S. Li, Z. Qiao, L. Cheng, C. Wang, K. Meng, G. Chen, *Energy Technol.* **2020**, *8*, 2000224.
[28] H. Yao, Y. Xu, G. Zhang, H. Lu, J. Zhu, M. Lyu, Y. Ding, *Adv. Funct. Mater.* **2023**, *33*, 2302162.
[29] C. C. Chang, J. H. Tao, C. E. Tsai, Y. J. Cheng, C. S. Hsu, *ACS Appl. Mater. Interfaces* **2018**, *10*, 21466.
[30] S. Daskeviciute-Geguziene, A. Magomedov, M. Daskeviciene, K. Genevicius, N. Nekrasas, V. Jankauskas, K. Kantminiene, M. D. McGehee, V. Getautis, *Chem. Commun.* **2022**, *58*, 7495.
[31] Q. Wang, Z. Lin, J. Su, Y. Xu, X. Guo, Y. Li, M. Zhang, J. Zhang, J. Chang, Y. Hao, *EcoMat* **2022**, *4*, e12185.
[32] J. Zhang, X. Zheng, Q. Cui, Y. Yao, H. Su, Y. She, Y. Zhu, D. Li, S. Liu, *Adv. Funct. Mater.* **2024**, *34*, 2404816.
[33] S. Liu, V. P. Biju, Y. Qi, W. Chen, Z. Liu, *NPG Asia Mater.* **2023**, *15*, 27.
[34] N. Y. Nia, F. Matteocci, L. Cina, A. Di Carlo, *ChemSusChem* **2017**, *10*, 3854.
[35] Y. Sun, Y. Wu, X. Fang, L. Xu, Z. Ma, Y. Lu, W. H. Zhang, Q. Yu, N. Yuan, J. Ding, *J. Mater. Chem. A* **2017**, *5*, 1374.
[36] Y. Chen, Z. Yang, S. Wang, X. Zheng, Y. Wu, N. Yuan, W. H. Zhang, S. Liu, *Adv. Mater.* **2018**, *30*, 1805660.